Chinese Journal of Aeronautics, (2015),28(1): 121–132

Chinese Society of Aeronautics and Astronautics
& Beihang University

Chinese Journal of Aeronautics

cja@buaa.edu.cn
www.sciencedirect.com

Thermal protection mechanism of heat pipe in leading edge under hypersonic conditions

Peng Wengen [a], He Yurong [a,*], Wang Xinzhi [a], Zhu Jiaqi [b], Han Jiecai [b]

[a] School of Energy Science & Engineering, Harbin Institute of Technology, Harbin 150001, China
[b] Center for Composite Materials, Harbin Institute of Technology, Harbin 150001, China

Received 17 February 2014; revised 5 April 2014; accepted 23 May 2014
Available online 26 December 2014

KEYWORDS

Aerodynamic heating;
Hypersonic vehicles;
Metallic heat pipe;
Thermal protection;
Thermoanalysis

Abstract Sharp local structure, like the leading edge of hypersonic aircraft, confronts a severe aerodynamic heating environment at a Mach number greater than 5. To eliminate the danger of a material failure, a semi-active thermal protection system is proposed by integrating a metallic heat pipe into the structure of the leading edge. An analytical heat-balance model is established from traditional aerodynamic theories, and then thermal and mechanical characteristics of the structure are studied at Mach number 6–8 for three refractory alloys, Inconel 625, C-103, and T-111. The feasibility of this simple analytical method as an initial design tool for hypersonic aircraft is assessed through numerical simulations using a finite element method. The results indicate that both the isothermal and the maximum temperatures fall but the von Mises stress increases with a longer design length of the leading edge. These two temperatures and the stress rise remarkably at a higher Mach number. Under all investigated hypersonic conditions, with a 3 mm leading edge radius and a 0.15 m design length, the maximum stress exceeds the yield strength of Inconel 625 at Mach numbers greater than 6, which means a material failure. Moreover, both C-103 and T-111 meet all requirements at Mach number 6–8.

1. Introduction

Hypersonic aircraft, such as ballistic missiles, cruise missiles, reentry vehicles, trans-atmosphere aerospace aircrafts, etc., usually fly at a Mach number greater than 5 under a high-altitude/low-density working condition in the atmosphere.[1,2] Due to a series of outstanding advantages of superior maneuverability, high level of survivability and excellent global strike capability, it has become a major research field in aeronautics and astronautics worldwide.[3–5]

In order to reduce aerodynamic resistance, an extremely sharp wing leading edge is required and a radius with a magnitude of millimeters is commonly employed.[6–8] In contrast to traditional subsonic and supersonic conditions, since the speed of hypersonic aircraft has been raised significantly, high temperature becomes one of the vital features, as most of the kinetic energy of the high speed airflow, just outside the sharp local structure, transforms into internal energy.[9] This

* Corresponding author. Tel.: +86 451 86413233.
E-mail address: rong@hit.edu.cn (Y. He).

Peer review under responsibility of Editorial Committee of CJA.

Production and hosting by Elsevier

http://dx.doi.org/10.1016/j.cja.2014.12.018
1000-9361 © 2015 Production and hosting by Elsevier Ltd. on behalf of CSAA & BUAA.

is the result of a strong action of compression, friction and viscous dissipation, and it makes heat flux transmitted into the leading edge becomes intense. For instance, the temperature of the air flowing along the outer wall, which is believed to attain a stagnation state, reaches up to 1650–2650 °C ranging from Mach number 6 to 8. This makes the service environment of hypersonic aircraft deteriorate quickly, which easily leads to a failure of material.

Since thermal management has become one of the critical tasks of hypersonic aircraft, several types of strategies have been proposed to deal with such thermal protection problems concerning high speed phenomenon, such as ablative alloys, metal matrix composites, carbon/carbon composites, ultra-high temperature ceramics (UHTC), transpiration cooling systems, and film cooling systems.[7,10–14] To balance aerodynamic drag and aerothermal heating of a sharp leading-edge structure, an extra internal cooling system may be necessary.[15] The concept of applying a heat pipe has been supported by some academic achievements. Niblock et al.[16] evaluated four thermal protection systems (TPS) including a heat-pipe design and three other alternatives (ablative design, coated columbium, and a carbon–carbon high-temperature segment), and pointed out that the heat pipe yielded positive evidence of system integrity and was much less expensive on the basis of total program costs. Colwell and Modlin[17] indicated that it is helpful to limit the maximum surface temperature of the leading edge and moderate the gradients with a combination of a liquid metal heat pipe and surface mass transfer cooling techniques. Glass et al.[18] fabricated a leading-edge-shaped heat pipe with lithium as the actuating medium and tested its start-up characteristics in a vacuum chamber.

In this work, a semi-active thermal protection system, shown in Fig. 1, is proposed by integrating a metallic heat pipe into the structure of a leading edge, where q_{in} and q_{out} are the inward and outward heat flux, respectively. It is not until 1963 that a heat pipe was first demonstrated as an efficient heat-transfer device by Grover et al.[19] at Los Alamos National Laboratory, which arose a wide and serious attention on applying heat pipe in the heat-transfer engineering. Cotter[20] systematically established the quantitative engineering theory for the design and performance analysis of heat pipes and laid the foundation for the further rapid development in 1965. With an excellent isothermal quality and an ultra-high conductivity in excess of 100 times or even 1000 times that of copper at the same size, a heat pipe is widely utilized as a temperature control device in the field of aeronautics and space.[21,22] Owing to low melting points and a better capacity of heat transmission than common liquids, alkali metals (such as lithium, sodium and potassium) are satisfactory choices of actuating media for heat pipes and are effectively used in ultra-high temperature areas, like the thermal protection of hypersonic aircraft.

2. Mathematical model

2.1. Theoretical analysis

The Mach number Ma under investigation ranges from 6 to 8, which is generally the highest speed of aircraft when using hydrocarbon fuels.[23] As a constant dynamic pressure on the hypersonic aircraft, usually 48 kPa, has been confirmed in the atmosphere, the far-field temperature T_∞, pressure p_∞, and density ρ_∞ of the free airflow can be obtained from the fight height corresponding to a specific Mach number via the U.S. Standard Atmosphere.[24] All thermophysical properties of the atmosphere at Ma 6–8 are summarized in Table 1, T_{st} is the stagnation point temperature.

By converting all the kinetic energy of the high-speed airflow into internal energy in an isentropic process, state parameters can be obtained at the stagnation point, which is located just in front of the sharp tip of the leading edge. The stagnation enthalpy H_{st} of the air is a function of the temperature and the aircraft velocity:

$$H_{st} = c_p T_\infty + u_\infty^2/2 \tag{1}$$

where c_p is the specific heat of air and equals 1.04 kJ/(kg·°C), u_∞ is the aircraft velocity.

On the basis that the stagnation pressure p_{st} is much greater than p_∞, i.e., $p_{st} \gg p_\infty$, p_{st} can be approximated by ignoring p_∞ as follows:

$$p_{st} \approx \rho_\infty u_\infty^2 \tag{2}$$

The cross section of the leading edge consisting of an inner heat pipe with a design length L (the length of the straight portion of the heat pipe starting from the junction of the curved and flat surfaces) and an outer metal layer, exposed to intense aerodynamic heating, with a thickness t is sketched in Fig. 2. The outer layer is a solid structure of one of the three refractory alloys, named the nickel based alloy Inconel 625, the niobium based alloy C-103, and the tantalum based alloy T-111. Physical and mechanical properties of these three alloys are summarized in Table 2 and temperature-dependent ones are given at 800 °C. The sharp curved tip, followed by a wide flat plane, has an outer radius R_{le} and an expansion angle φ_0 (complementary of the half wedge angle θ).

Under a strong action of aerodynamic heating, the whole system of the leading edge attains thermodynamic equilibrium under a heat transfer process described as follows. When the high-speed airflow encounters the structure of the leading edge,

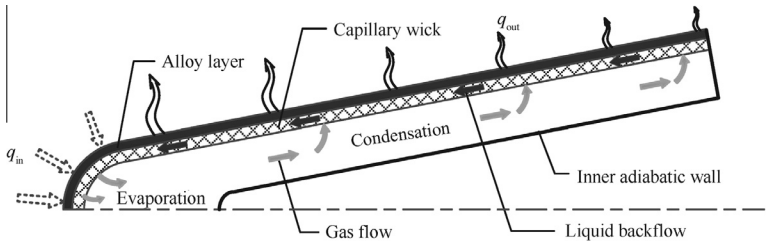

Fig. 1 Schematic structure of a heat pipe attached to an outer alloy in a leading edge.

Table 1 Standard atmosphere properties and stagnation state parameters.

Ma	Altitude (km)	T_∞ (K)	p_∞ (Pa)	ρ_∞ (kg/m^3)	u_∞ (km/s)	H_{st} (MJ/kg)	T_{st} (K)
6	26.93	223.5	1900	0.0296	1.54	1.80	1651
7	28.98	225.5	1396	0.0215	2.11	2.16	2122
8	30.76	227.3	1069	0.0160	2.42	2.86	2627

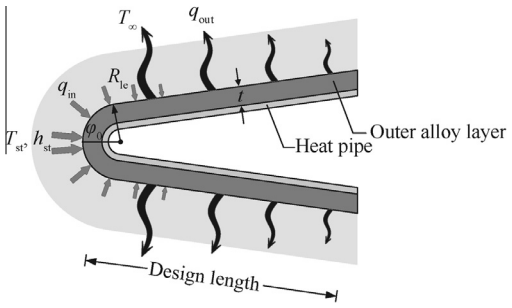

Fig. 2 Structure of leading edge and thermal boundary condition.

it is assumed that the air near the outer wall reaches its stagnation state and has a temperature of T_{st}. Mainly via the sharp tip region, the generated aerothermal heat enters the structure in the form of convection, of which the heat transfer coefficient varies as a function of spatial location along the outer surface. Then the heat is conducted through the metal structure into the inner high-temperature heat pipe, where it is quickly transferred to the following wide-flat wall as a result of an efficient evaporation and condensation process of the actuating medium. Finally the heat is radiated into the low temperature surrounding environment along the total surface of the leading edge.

Many empirical engineering formulas are proposed to estimate the heat transfer rate at the stagnation point. These form the basis of aerodynamic investigations into heating phenomena under hypersonic conditions. Fay and Riddell[25] proposed a widely adopted heat flux formula at the stagnation point:

$$q = 0.763 Pr^{-0.6} \left(\frac{\rho_w \mu_w}{\rho_{st} \mu_{st}}\right)^{0.1} \sqrt{\rho_{st}\mu_{st}\left(\frac{dV_e}{dx}\right)_{st}} \cdot \left[1 + (Le^{0.52} - 1)\frac{H_D}{H_{st}}\right](H_{st} - H_w) \quad (3)$$

where Pr is the Prandtl number, ρ the density of air, μ the viscosity of air, H the enthalpy, Le the Lewis number, and suffixes "st", "w" and "D" represent the stagnation point, wall and dissociation state, respectively.

Under the hypersonic conditions investigated, as the enthalpy of air at the stagnation point equals H_{st} and $H_{st} \gg H_w$, Sutton and Graves[26] give the following cold wall ($H_w = 0$) correlation derived from the formula of Fay and Riddell:

$$q_{st}|_{cw} = H_{st} K \sqrt{P_{st}/R_{le}} \quad (4)$$

Based on the work of Svehla,[27] Sutton and Graves approximate $K = 3.6 \times 10^{-4}$ kg$^{1/2}$/m for air. Thus, the heat transfer coefficient at the stagnation point becomes:

$$h_{st} = q_{st}|_{cw}/T_{st} \quad (5)$$

As mentioned above, the convective heat transfer coefficient h is a spatial function along the outer surface of the leading edge. For a curved surface, a theoretical basis of the cosine variation of heating at least to the structure sonic point (near 45°) can be found in the work of Lees.[28] Although it is approximate, Tauber[29] further points out that the cosine variation gives reasonable results beyond the stagnation point. Consequently, a cosine function of φ is applied for the convective heat transfer coefficient h in this work, i.e., $h(\varphi) = h_{st}\cos\varphi$. The aerodynamic heat entering the leading edge through the curved region can be obtained by integrating the heat transfer coefficient $h(\varphi)$ along the outer surface. The thermal boundary assumptions are that the alloy structure reaches an isothermal temperature T_{iso} and that the air temperature outside the leading edge reaches T_{st}:

$$Q_{in}^c = \int_0^{\varphi_0} R_{le} h(\varphi)(T_{st} - T_{iso}) d\varphi = R_{le} h_{st} \sin\varphi_0 (T_{st} - T_{iso}) \quad (6)$$

For the wide flat region, a sketch of the geometry and related parameters is shown in Fig. 3 for the calculation of the heat transfer coefficient along the outer surface, which has a decreasing trend as $h(s) \sim 1/\sqrt{s}$, proposed by Lees[28] and Bertin.[30] To maintain a continuity of h between the curved and flat regions, h must be identical at the junction of these two parts. The following formula gives the heat transfer coefficient along the outer surface:

$$h(s) = h_{st} \cos\varphi_0 \sqrt{R_{le}/(s\tan\theta)} \quad (7)$$

where s is the distance from the intersection point of the upper and lower surfaces of the leading edge, and θ is the half wedge angle.

The dimensionless heat transfer coefficient h/h_{st} as a function of S/R_{le} is shown in Fig. 4 with (a) a linear scale and (b) a logarithm scale in the abscissa axis, where the S in this

Table 2 Physical and mechanical properties of refractory alloys Inconel 625, C-103, and T-111.

Material	ρ (kg/m^3)	c_p (J/(kg·°C))	k (W/(m·°C))	a (10^{-6}/°C)	E (GPa)
Inconel 625	8440	600.8	21.5	15.5	153.0
C-103	8850	343.0	37.4	7.4	72.8
T-111	16720	210.0	53.4	6.7	163.9

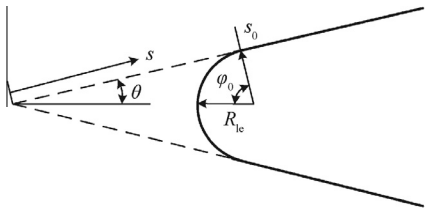

Fig. 3 Sketch of geometry and related parameters for calculation of heat transfer coefficient along flat surface (dashed lines with an intersection represent the extension of the flat surface).

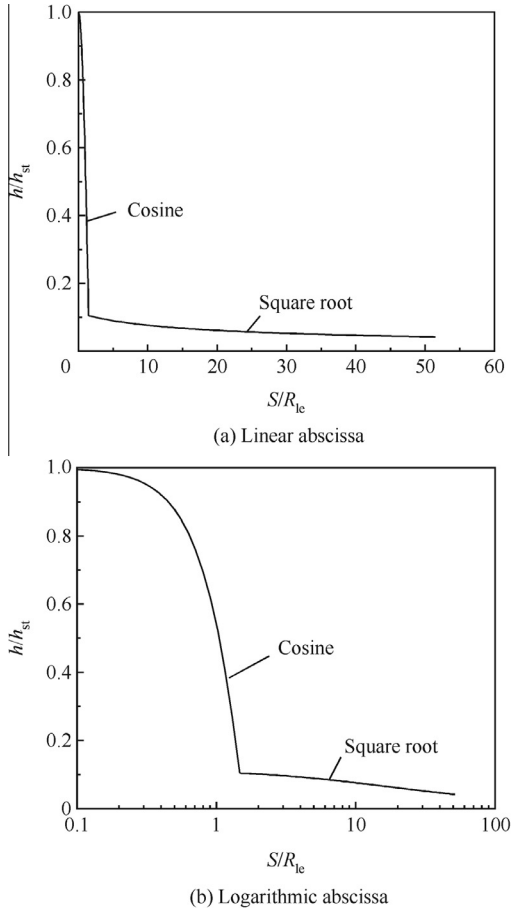

Fig. 4 Dimensionless heat transfer coefficient as a function of the distance along outer surface from stagnation point.

figure means the distance along the outer surface of the leading edge from stagnation point. It is found that this dimensionless heat transfer coefficient is independent from the Mach number (flight speed). The heat transfer coefficient and the temperature difference between the leading edge and the air determine the total inward heat flux. The aerodynamic heat entering the flat region is

$$Q_{in}^{f} = \int_{s_0}^{s_0+L} h(s)(T_{st} - T_{iso})\mathrm{d}s = \frac{2h_{st}\cos\varphi_0\sqrt{R_{le}}}{\tan\theta}\left(\sqrt{R_{le} + L\tan\theta} - \sqrt{R_{le}}\right)(T_{st} - T_{iso}) \quad (8)$$

In the process of hypersonic flow over the blunt-nose structure, as all the heat absorbed is radiated into the cold environment in the end, the consideration of the heat transfer regime of radiation is important to thermal protection systems.[31,32] This makes the emissivity ε of a material become an important parameter that controls the amount of outward heat. Although the emissivity of traditional alloys is relatively low, a high value greater than 0.9 could be achieved by forming a thin membrane of Al_2O_3 or SiO_2 on the surface of refractory alloy. Therefore, a fixed emissivity $\varepsilon = 0.9$ is used in all analyses in this work. The total outward heat radiated from the whole surface of the leading edge is obtained as follows:

$$Q_{out} = \int_0^{L_{tot}} \varepsilon\sigma\left(T_{iso}^4 - T_\infty^4\right)\mathrm{d}s = \varepsilon\sigma L_{tot}\left(T_{iso}^4 - T_\infty^4\right) \quad (9)$$

where σ is the Boltzmann constant which equals 5.67×10^{-8} W/(m^2·K^4), $L_{tot} = R_{le}\varphi_0 + L$ is the total length of the heat pipe. After the whole system reaches a state of thermodynamic equilibrium where $Q_{in} = Q_{out}$, a fourth power formula of T_{iso} as a function of the leading edge dimension and flight conditions is given as follows:

$$R_{le}h_{st}\sin\varphi_0(T_{st} - T_{iso}) + \frac{2h_\varphi\sqrt{R_{le}}}{\tan\theta}\cdot\left(\sqrt{R_{le} + L\tan\theta} - \sqrt{R_{le}}\right) \cdot (T_{st} - T_{iso}) - \varepsilon\sigma L_{tot}\left(T_{iso}^4 - T_\infty^4\right) = 0 \quad (10)$$

To find the maximum temperature in the leading edge, an infinitesimal element $R_{le}\mathrm{d}\varphi$, shown in Fig. 5, is selected. A one-dimensional annulus heat conduction model is used to describe the steady-state-heat-transfer process within the sharp tip. The differential equation is

$$k\left(\frac{\partial^2 T}{\partial r^2} + \frac{1}{r}\cdot\frac{\partial T}{\partial r}\right) = 0 \quad (11)$$

where k is the thermal conductivity of solid material, and r the radius starting from the center of curved part. Depending on the inner temperature T_{iso}, the maximum temperature T_{max} on outer surface is

$$T_{max} = \frac{T_{iso} + T_{st}\left(\frac{R_{le}h_{st}}{k}\ln\frac{R_{le}}{R_i}\right)}{1 + \frac{R_{le}h_{st}}{k}\ln\frac{R_{le}}{R_i}} \quad (12)$$

where $R_i = R_{le} - t$ is the inner radius.

Safety of the whole system is determined by the difference between the maximum stress σ_v in the leading edge and the yield strength σ_s of the material at the same temperature. Taking the reference temperature as T_{iso} and neglecting the effect of the shear stress, the von Mises stress σ_v is

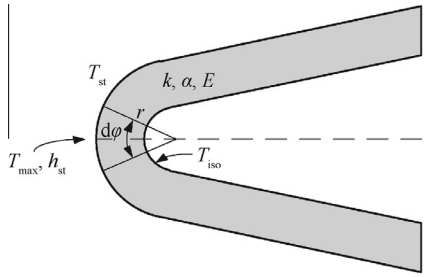

Fig. 5 A one-dimensional annulus model of heat conduction.

$$\sigma_v = \alpha E(T_{st} - T_{iso}) \frac{\frac{R_{le}h_{st}}{k}\ln\frac{R_{le}}{R_i}}{1 + \frac{R_{le}h_{st}}{k}\ln\frac{R_{le}}{R_i}} \quad (13)$$

2.2. Finite element method

The one-dimensional theoretical analysis has the advantage of brevity and is less time-consuming than other methods, but its precision needs to be validated. In order to determine whether the theoretical analysis is accurate enough for an initial engineering design, numerical simulations are carried out using a finite element method in a 2D Cartesian coordinate system.

After an overall study of the characteristics of the structure and the aerodynamic heat transfer process, it is believed that a remarkable variation of thermal physical parameters, such as the temperature, the heat flux and the stress, is presented across the section of a leading edge within a narrow area. Uniform distributions of these parameters are also found in the extremely wide wing-span direction. Therefore, a simplified 2D model is proposed to investigate the heat transfer process and thermal protection of the leading edge.

Fig. 6 gives the schematic structure of the leading edge in solid lines in the upper left corner and the sizes of the leading edge are summarized in Table 3. A finite element method is utilized to solve the problem, and two layers of coupled-field quadrilateral meshes are generated for the structure of the leading edge and the heat pipe. The local mesh near the sharp top is shown in the lower right corner, within which the outer black mesh represents a refractory alloy and the additional grey mesh, attached to the inner surface of leading edge, is utilized to cover the effect of the liquid metal heat pipe with a thickness of 1 mm and an extra high conductivity k_{eff}. Since a conductivity more than 100 times that of copper has been reported, k_{eff} = 39800 W/(m·°C) is used for the heat pipe in all the simulations. Finally the effect of emissivity is considered using a thermal-surface-effect element attached to the outer surface of the leading edge. As a computational work, the

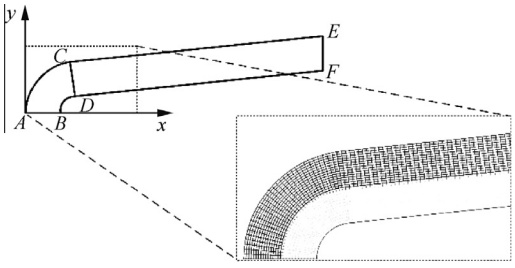

Fig. 6 2D schematic of the structure and local mesh near top tip of leading edge.

Table 3 Structure dimensions of leading edge.

Structure	Size
Outer radius R_{AC} (R_{le}) (mm)	3
Inner radius R_{BD} (mm)	1
Total thickness L_{AB} (mm)	2
Design length L (m)	0.15
Angle between AB and CD φ_0 (°)	84

Table 4 Grid schemes used in verification and validation processes.

Grid	*AB*	*AC*	*CE*
Very coarse	4	4	60
Coarse	13	16	270
Standard	27	32	540
Fine	54	64	1080

verification and validation processes for this numerical method are imperative. Four types of grid schemes are used for the verification process and their cells number is given in Table 4. The results of the grid independence study are demonstrated in Section 3.2.

The same thermal boundary conditions as those in the analysis section are applied to the numerical simulation. Details on the leading edge, represented by *AB*, *AC*, etc. line segments in Fig. 6, are expressed as follows.

(1) *AB* and *EF*: symmetric boundary, displacements of *AB* and *EF* are constrained to zero in the y and x directions, respectively.
(2) *BD* and *DF*: adiabatic boundary, no heat passes through these two faces.
(3) *AC* and *CE*: convective boundary, *AC* and *CE* are subject to a space-varying heat transfer coefficient the same as $h(\varphi)$ and $h(s)$ in the theoretic analysis section to estimate the total inward heat.
(4) *AE*: radiating boundary, *AE* has a surface emissivity $\varepsilon = 0.9$ and an environment temperature T_∞ according to a specific Mach number to calculate the total outward heat from the leading edge.

3. Results and discussion

3.1. Analytical results

Under an intense aerodynamic heating phenomenon and a widespread cooling effect of radiating extra heat into the low temperature atmosphere, the whole system reaches a state of heat balance. Because of a high thermal conductivity of the outer refractory alloy layer and the good isothermal quality of the high-temperature heat pipe, an equivalent temperature, named T_{iso}, is believed to be achieved on most parts of the leading edge except at the sharp curved top. One function of T_{iso} is treated as the reference temperature for choosing an actuating medium for the heat pipe, which makes it a very important parameter.

Dimensionless analytical results of T_{iso}/T_∞ are shown in Fig. 7 as a function of L/R_{le} at different Mach numbers for three refractory alloys, namely the Inconel 625, the C-103, and the T-111. In this work, an outer radius R_{le} of 3 mm and a half wedge angle θ of 6° are fixed for all investigations. It is obvious from Fig. 7 that T_{iso}/T_∞ ranges widely and is unaffected by the choice of materials of the leading edge. In all cases, T_{iso} is higher than 800 °C and even reaches up to a high value near 1550 °C at $Ma = 8$, which exceeds the temperature limit of most common materials. This partly shows a severe aerothermal environment of the leading edge. Also, the flight speed of hypersonic aircraft has a strong influence

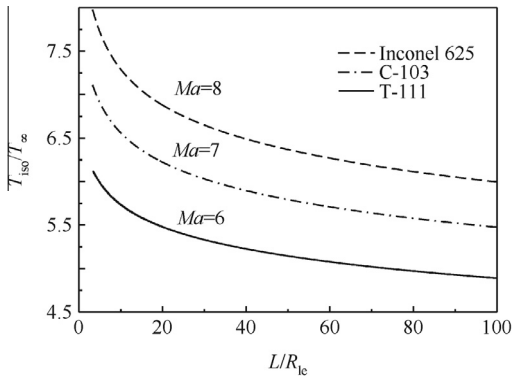

Fig. 7 Dimensionless analytical isothermal temperature of the leading edge.

on T_{iso}/T_∞ with an increase of 0.5 to 1.0 when the Mach number rises by 1 unit. Another conclusion obtained is that T_{iso}/T_∞ is sensitive to the design length L/R_{le}. T_{iso}/T_∞ decreases rapidly with a longer L/R_{le}, especially in the short length region.

In view of the structure sizes and the manufacturing convenience of the leading edge, a design length $L = 0.15$ m is chosen as the standard value in the following numerical simulation section. With this specific design length, analytical results of 876.7, 1033.3, 1174.3 °C are obtained for T_{iso} from $Ma = 6$–8. As the start-up temperature of a heat pipe is low compared to the boiling point of its actuating medium, the alkali metal lithium is selected according to the T_{iso} in this work, since it has a low melting point of 180.5 °C and a boiling point of 1347 °C. This assures the simultaneous presence of the gas and liquid phases, which is essential for the normal operation of a heat pipe.

The maximum temperature T_{max} is determined by the structure size, the thermal conductivity, the isothermal temperature, and Mach number. As the highest temperature in the leading edge, the spot, where T_{max} occurs, is the most dangerous place. Therefore, it is important in the design of hypersonic aircraft to ascertain the influencing factors and figure out methods of decreasing the temperature.

The influence of L/R_{le} and Ma on T_{max}/T_∞ is shown in Fig. 8 for three materials, Inconel 625, C-103, and T-111. With an identical design length and flight speed, a good phenomenon is illustrated in Fig. 8 that a higher thermal conductivity leads to a lower T_{max}. Among these three alloys, the difference in temperature reaches a maximum with L/R_{le} of 100 at $Ma = 8$, where T_{max}/T_∞ of C-103 and T-111 are respectively lower by 3.1% and 4.6% than Inconel 625, while their conductivities are significantly higher at 74% and 148%. This means that the conductivity of a material only has a relatively low influence on T_{max}.

Similar to the isothermal temperature T_{iso}, the design length L and the Mach number have a strong impact on T_{max}, and a lower value of T_{max} is obtained due to a longer L or a smaller Mach number. T_{max} in the structure of Inconel 625 reaches up to 931 °C($Ma = 6$), 1116 °C($Ma = 7$), and 1299 °C($Ma = 8$) with a design length of 0.15 m. It shows an increase of 185 °C and 368 °C for $Ma = 7$ and 8 respectively compared to that of $Ma = 6$, which directly demonstrates that the aerothermal environment of hypersonic aircraft worsens quickly at a higher Mach number. Combined with Fig. 7, it shows that T_{max}/T_∞ only deviates a little from T_{iso}/T_∞.

Without a heat pipe, the structure of leading edge does not achieve an isothermal temperature. Still, temperature distributes uniformly through the thickness, but varies along the length of the outer surface. In order to investigate the characteristic of heat transfer in absence of a heat pipe, a one-dimensional differential equation for lengthwise square elements is given as follows to describe the temperature distribution of T-111 at $Ma = 6$, as shown in Fig. 9.

$$\frac{d^2T(S)}{dS^2} = \frac{1}{kt}\left\{\varepsilon\sigma\left[T(S)^4 - T_\infty^4\right] - h(S)[T_{st} - T(S)]\right\} \tag{14}$$

It can be seen from Fig. 9 that the highest temperature occurs at the stagnation point ($S/R_{le} = 0$) of the outside surface. Differing completely from the heat-pipe cases, the maximum temperature is almost independent from the design length L and T/T_∞ reaches a constant value of about 6.27. A longer L will decrease the minimum temperature, which means a greater temperature difference is present. For example, the dimensionless temperature difference employing T-111 is 1.37 in the case of 0.08 m L at $Ma = 6$, much higher than the value of 0.1 that arises in the presence of a heat pipe under the same conditions. A greater temperature difference will significantly arouse the thermal stress, which indicates that it is helpful to decrease the thermal stress and establish a much safer condition for hypersonic aircraft by integrating a heat pipe into the structure of the leading edge, due to its excellent capability of heat transfer and isothermal characteristics.

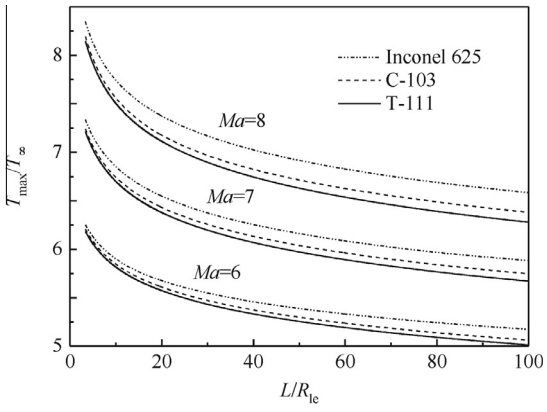

Fig. 8 Dimensionless maximum temperature of leading edge.

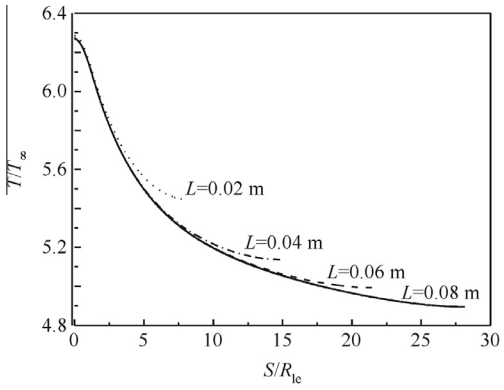

Fig. 9 Dimensionless temperature of leading edge without a heat pipe ($Ma = 6$, T-111).

Fig. 10 shows the dimensionless maximum von Mises stress σ_v/E in the structure as a function of design length L/R_{le} at different Mach numbers. As seen from the figure, σ_v/E increases with a longer L/R_{le}. This is because if L/R_{le} increases, although the temperature declines, a greater temperature difference between the structure and the surrounding thermal environment is found, consequently with more heat getting into the structure, a greater temperature gradient is needed to transfer the heat flux.

The above analysis shows that T_{max}/T_∞ is only slightly affected by the choice of materials; however, a strong correlation of σ_v/E with different materials is found here. σ_v/E of C-103 does not exceed 0.61 even under the most severe condition at $Ma = 8$ with a L/R_{le} of 100, while a value of 1.86 is found for Inconel 625. This is due in part to the fact that σ_v/E has a linear correlation of the thermal expansion α. That means a higher conductivity, a lower thermal expansion, and a lower elastic modulus will help to decrease the von Mises stress in the leading edge.

The temperature-dependent yield strength of the three refractory alloys is illustrated by solid lines on the left in Fig. 11(a). Analytical results of the von Mises stress, in the lower-right corner, are shown for each material at each Mach number. Fig. 11(b) illustrates a partial enlarged detail of the lower-right corner to clearly shows comparison between the von Mises stress and the strength of each alloy at the same temperature. The maximum temperature corresponding to the shortest L/R_{le} of 3.3, which means the most dangerous situation investigated, is summarized in Table 5. The von Mises stress and the yield strength at that temperature are also given. However, no yield strength exists if the calculated temperature goes near or exceeds the melting point of the material. With regard to Inconel 625, the von Mises stress generated in the structure does not exceed the material strength at a speed of $Ma = 6$, but it immediately goes beyond the safe region as the Mach number rises to 7 and a failure occurs. Good safety margins for C-103 and T-111 are obtained in the whole range of Mach numbers under investigation.

Comparing the thermal and mechanical properties of these three alloys in Table 2, it indicates the high thermal conductivity of C-103 and T-111 is the reason that reduces their maximum temperature and stress. Although yield strength of Inconel 625 is greater than that of C-103, a much higher von Mises stress brings about a material failure instead. Hence,

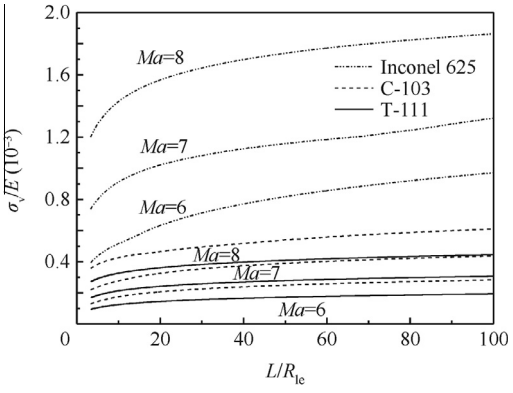

Fig. 10 Dimensionless analytical von Mises stress of leading edge.

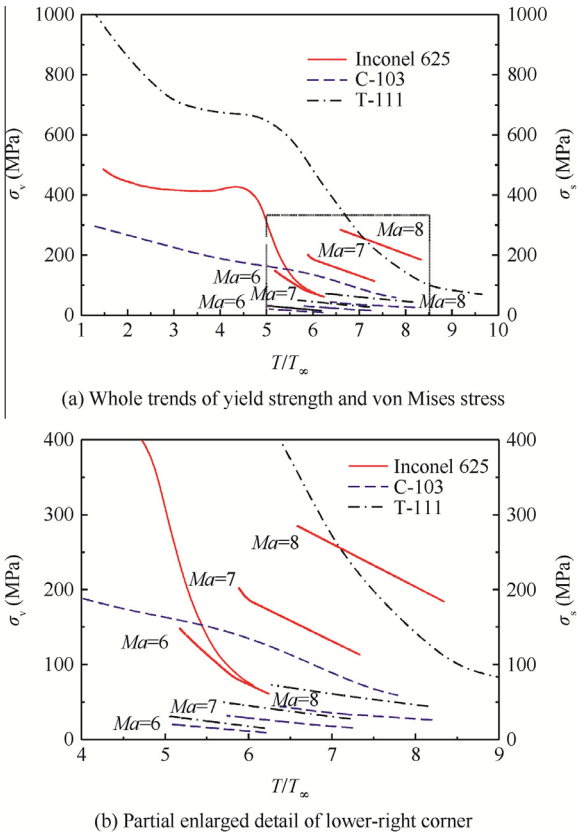

Fig. 11 Yield strength and von Mises stress of Inconel 625, C-103 and T-111.

Table 5 Summary of the maximum temperature, the von Mises stress, and yield strength corresponding to $L/R_{le} = 3.3$.

Material	*Ma*	T_{max} (°C)	σ_v (MPa)	σ_s (MPa)
Inconel 625	6	1124.1	60.5	
	7	1381.4	112.9	
	8	1624.1	183.9	
C-103	6	1114.3	9.4	133.0
	7	1359.9	15.9	75.0
	8	1589.2	26.1	
T-111	6	1109.4	15.4	451.0
	7	1353.3	27.7	235.9
	8	1578.5	44.4	118.5

the yield strength of a material is not the only factor that needs to be considered. As mentioned above, a longer L will lead to a reduction of temperature. This is followed by a move of the von Mises stress towards the left part (lower temperature but higher stress) in Fig. 11, which indicates a safer margin as materials quickly weaken at higher temperatures.

3.2. Numerical simulation

To provide a reference to the previous analytical work, a finite element method is utilized here to investigate the temperature distribution of the outer alloy layer of the leading edge, shown

in Fig. 12. The whole flat region and the inner part of the curved region nearly reach a uniform temperature, which confirms the previous hypothesis that the whole leading edge except the sharp tip area achieves an isothermal temperature, identified as T_{iso}. An obvious variation of the temperature is shown within the local area of the sharp tip and a higher temperature is found when getting closer to the outer surface, with a maximum achieved at the stagnation point.

The verification and validation processes are conducted for the numerical method. With the four grid schemes given in Table 4, the corresponding results of the grid independence study are shown in Fig. 13. The temperature distribution along the outer surface is obtained with different grid schemes. It is found that the discrepancy of temperature between different grid schemes is negligible except a small underestimation with the very coarse grid. This means the default standard grid in this work is enough for numerical prediction.

The temperature distribution along the outer surface of C-103 is illustrated by solid lines at Ma = 6–8 in Fig. 14, the two dashed lines across the figure represent the analytical T_{iso}/T_∞ and T_{max}/T_∞ obtained from the work above. A sharp gradient of the temperature is found from the stagnation point (S/R_{le} = 0) towards its vicinity at the joining ($S/R_{le} \approx 1.6$) between the curved front and the flat rear surface. From then on the temperature declines at a low rate along the wide flat surface. This puts the front region in a bad situation as the thermal stress in the structure rises greatly caused by the sharp change of the temperature. These results show a satisfactory consistency

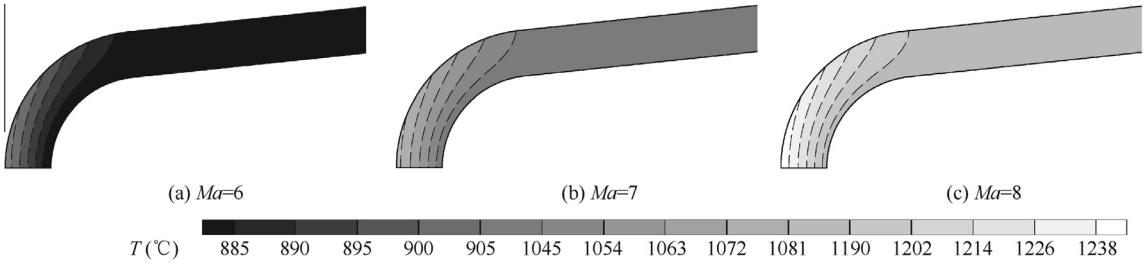

Fig. 12 Temperature distribution at variable Mach number (C-103, L/R_{le} = 50).

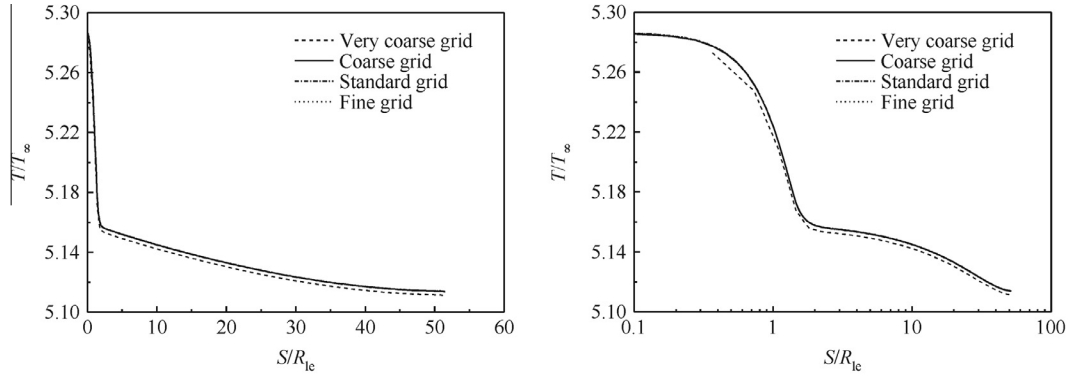

Fig. 13 Grid independency study (C-103, Ma = 6, L/R_{le} = 50).

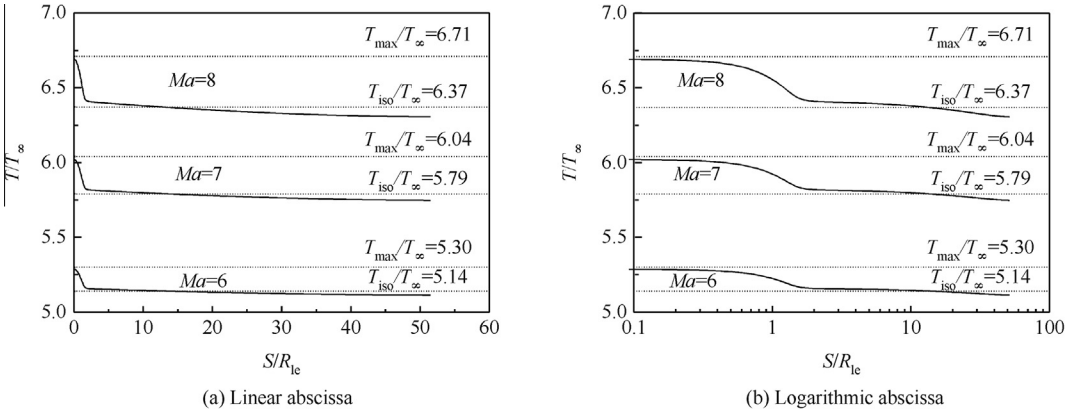

Fig. 14 Temperature along outer surface of leading edge (C-103, L/R_{le} = 50).

between the analytical and numerical results with the relative error of T_{max}/T_{∞} within 0.35% for Ma = 6–8. A more detailed comparison is summarized in Table 6. The fact that the analytical T_{iso}/T_{∞} falls in the middle of the wide temperature-slow-declining area means it is feasible to use T_{iso} as the average working temperature of the heat pipe for an initial design.

Fig. 15 shows the influence of the choice of materials on the outer surface temperature. The maximum temperatures at the stagnation point are somewhat different for these three alloys and the analytical results give T_{max}/T_{∞} of 6.92, 6.71, and 6.63 for Inconel 625, C-103, and T-111 respectively. The good agreement of the temperature between different materials along the wide flat surface supports the conclusion in the analytical section that T_{iso} is independent from materials.

To find out the effect of thermal protection, the temperature distribution with and with no heat pipe is shown in Fig. 16. Compared to that with a heat pipe, the dimensionless maximum temperature increases by 19.9%, 24.5%, and 28.5% at Ma = 6, 7, 8, respectively. As seen from the figure, there is no uniform temperature in the whole flat region of the leading edge when with no heat pipe. As the maximum temperature at the stagnation point greatly increases and the minimum temperature at the end of the leading edge remarkably decreases, a much wider distribution of temperature obviously turns up in the absence of a heat pipe. This undesirable huge temperature difference contributes greatly to thermal stress.

The heat flux distributions of C-103 are shown in Fig. 17. Because of the effects of the small-leading-edge radius of

Table 6 Analytical and numerical results of the dimensionless maximum temperature T_{max} (L/R_{le} = 50).

Ma	Material	T_{max} (°C)		Relative error (%)
		Numerical	Analytical	
6	Inconel 625	923.8	931.3	0.81
	C-103	908.5	911.1	0.29
	T-111	900.8	901.3	0.06
7	Inconel 625	1107.4	1116.2	0.79
	C-103	1084.7	1088.5	0.35
	T-111	1073.1	1073.4	0.03
8	Inconel 625	1285.7	1298.9	1.03
	C-103	1248.1	1252.9	0.38
	T-111	1233.8	1233.8	0

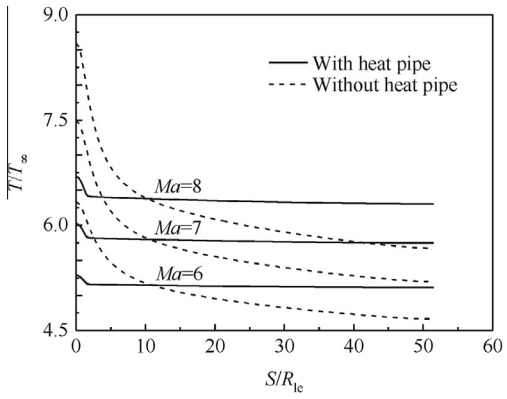

Fig. 16 Temperature distribution with and without heat pipe (C-103, L/R_{le} = 50).

3 mm and the strong aerodynamic heating through the curved region, the heat flux q is intense in this tip area. What is more, with a cumulative phenomenon of heat due to a decreasing radius via the alloy layer, a maximum q_{max} is achieved at the intersection of the symmetry line of the leading edge and the inner surface, with values of 1.33, 2.21, 3.31 MW/m^2 from Ma = 6 to 8.

The distribution of heat flux q/q_{st} and the total net heat Q_{net} of C-103 along the outer surface are illustrated in Figs. 18 and 19. A positive q/q_{st} means the heat transmitted from the atmosphere into the leading edge, while a negative one describes the opposite process. The three dimensionless heat flux q/q_{st} at different Mach numbers collapse into just one curve, which means q/q_{st} is independent of the freestream conditions or wall temperature level throughout the range of the investigations. By analyzing experimentally the heat transfer distribution to a circular cylinder normal to a supersonic air conditions, Tewfik and Giedt[33] proposed the following relation as an empirical fit to experimental data:

$$\frac{q}{q_{st}} = 0.37 + 0.48\cos\varphi + 0.15\cos 2\varphi \tag{15}$$

The heat flux results yielded by this expression are compared to those from numerical simulation for the cylindrical portion of the leading edge. From Fig. 18, the numerical simulation predicts a heat flux that almost equals results from the above empirical expression, especially near the stagnation point

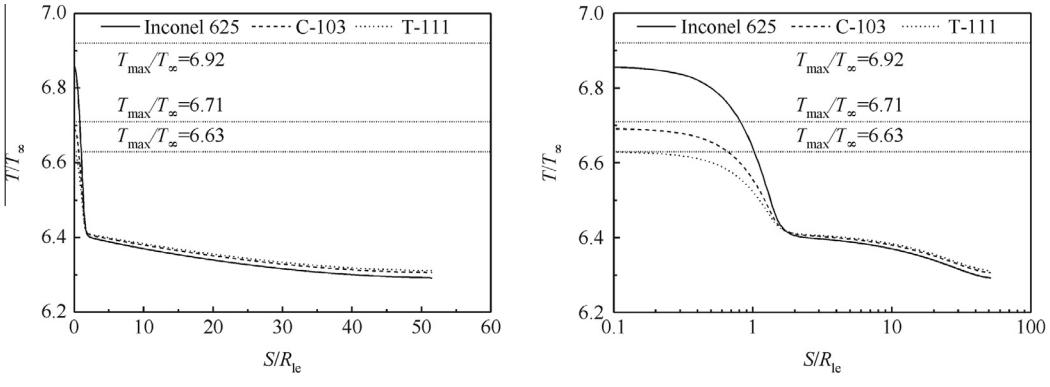

(a) Linear abscissa (b) Logarithmic abscissa

Fig. 15 Temperature along outer surface of Inconel 625, C-103 and T-111 (Ma = 8, L/R_{le} = 50).

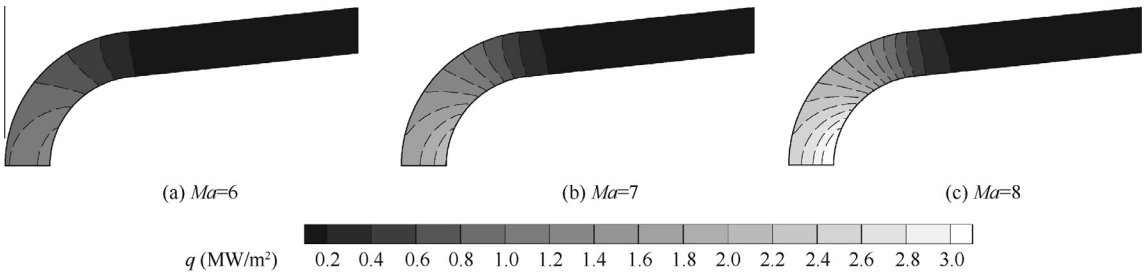

Fig. 17 Heat flux distribution at various Mach numbers (C-103, $L/R_{le} = 50$).

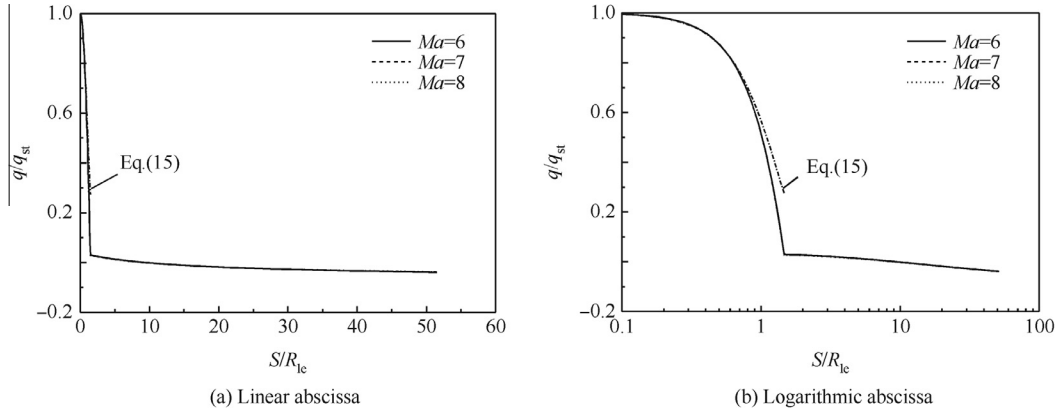

Fig. 18 Heat flux along the outer surface of leading edge (C-103, $L/R_{le} = 50$).

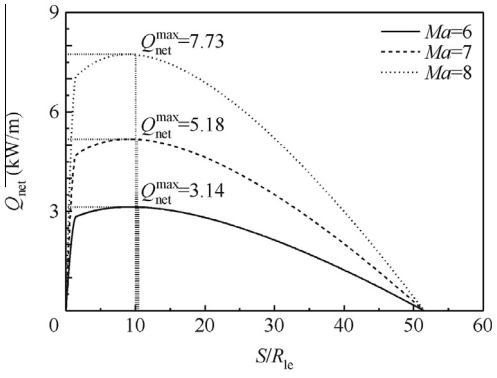

Fig. 19 Total net heat into the structure of leading edge along outer surface (C-103, $L/R_{le} = 50$).

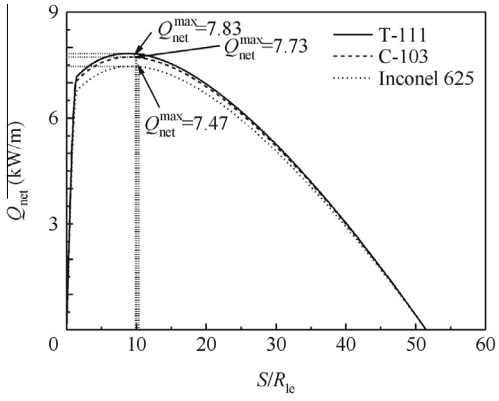

Fig. 20 Total net heat into the structure of Inconel 625, C-103 and T-111 along outer surface ($Ma = 8$, $L/R_{le} = 50$).

region. The relative error between numerical simulation and the empirical expression is less than 5% within the front 60% region, from the stagnation point, of the cylindrical portion.

Sharp gradients of q/q_{st} and Q_{net} corresponding with the change of temperature are found on the curved region, where an intense convective heat transfer process is present. A turning point is shown soon just behind of the joining of the two surfaces, then changes of these two parameters become slow. The cumulative heat Q_{net} has a zero value at the stagnation point ($S/R_{le} = 0$), due to a heat transfer of convection being much greater than that of radiation. A fast increase of Q_{net} happens until a maximum is reached near the turning point. Then the heat is slowly radiated into the cold surrounding environment over the wide flat surface. The whole structure reaches heat equilibrium when Q_{net} declines to zero at the end of the leading edge. Maxima of total net heat Q_{max} are 3.14, 5.18, 7.73 kW/m from $Ma = 6$ to 8, which shows an approximate proportionality to the third power of Ma, i.e., $Q_{max} \sim Ma^3$. Values of Q_{max} of Inconel 625, C-103, and T-111, shown in Fig. 20, are 7.47, 7.73, 7.83 kW/m respectively; it leads to a conclusion that the material contributes a little influence on the heat absorbed by the leading edge.

Q_{max} is a vital parameter for the design of the thermal protection system, as it is the maximum total heat that the heat pipe must transfer to offer an effective cooling. Unfortunately, as a vital heat transfer component, several heat transfer limits in the hypersonic area, such as sonic limit, capillary limit, and boiling limit, control the heat transfer capability of a heat pipe, which must endure Q_{max} generated in the structure for safety.

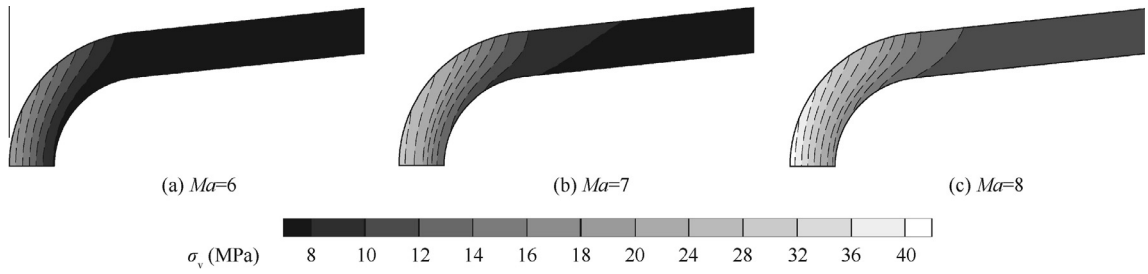

Fig. 21 Distribution of von Mises stress at variable Mach number (C-103, $L/R_{le} = 50$).

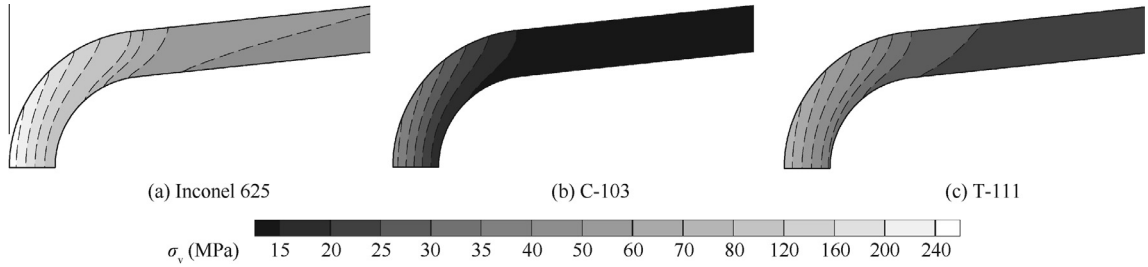

Fig. 22 Distribution of von Mises stress for Inconel 625, C-103 and T-111 ($Ma = 8$, $L/R_{le} = 50$).

The distributions of von Mises stress σ_v in the structure of C-103 are shown in Fig. 21. A clear relationship that the Ma number has a strong influence on the stress is presented. The maximum stress occurs at the stagnation point, the same place where T_{max} occurs, and has values of 19.4, 30.1, 42.2 MPa at $Ma = 6$–8. This is a relative enhancement of 55.2% and 40.2% with Ma increasing by 1 unit. Therefore, once the hypersonic aircraft speeds up, the stress increases significantly up to a dangerous value that gets close to or even exceeds the yield strength of the material. Commonly, a failure of material occurs as a result of the safety margin between the von Mises stress and the yield strength becoming so narrow, that as soon as the speed of hypersonic aircraft exceeds the design condition, it is likely for the stress to overstep the permissible extent.

The influence of materials on stress is shown in Fig. 22. Different materials affect stresses significantly and Inconel 625 has an extremely high maximum value of 264 MPa at $Ma = 8$, while C-103 and T-111 only show 42.2 MPa and 77 MPa respectively. One of the reasons for this phenomenon is that the von Mises stress σ_v has a strong relation with mechanical properties, such as the thermal expansion α and especially the Young's modulus E. The direct reason for the emergence of thermal stress is the temperature difference in the structure. As most of the leading edges reach a relatively uniform temperature, the maximum temperature T_{max} contributes greatly to the stress. Since the T_{max} of these three materials varies, σ_v in the structure of the leading edge differs significantly. Combined with Fig. 11, it can be seen that C-103 and T-111 are good choices of materials for the leading edge providing a wide safety margin. In view of being a light weight material, C-103 with a lower density (Table 2) is better than the heavy T-111.

3.3. Difference between theoretical analysis and numerical simulation

The analytical and numerical results of the maximum temperature T_{max} at different Mach numbers are given in Table 6 for Inconel 625, C-103, and T-111. Under all investigated conditions, it shows a perfect agreement of the analysis and the numerical simulation with all relative errors within 1%. This indicates that the analytical method is accurate enough to predict the temperature in the structure.

Table 7 Analytical and numerical results of the maximum stress σ_v ($L/R_{le} = 50$).

Ma	Material	σ_v (MPa)		Relative error (%)
		Numerical	Analytical	
6	Inconel 625	120.20	125.07	4.1
	C-103	19.44	18.12	6.8
	T-111	31.84	28.18	11.5
7	Inconel 625	177.62	177.25	0.2
	C-103	30.10	28.37	5.7
	T-111	52.05	45.66	12.3
8	Inconel 625	263.88	266.07	0.8
	C-103	42.22	39.26	7.0
	T-111	76.98	67.04	12.9

Differences in the maximum stress σ_v are summarized in Table 7 from $Ma = 6$ to 8 for these three materials. The estimates of the von Mises stress using theoretical analysis are satisfactory for Inconel 625 with all relative errors being less than 5%, but the results are not so good for C-103 and T-111 with a maximum relative error up to 12.9%. One possible reason for this is that the curve effect is not taken into account by the analytical method.

4. Conclusion

(1) Both the isothermal and the maximum temperatures fall but the von Mises stress increases under a longer design length of the leading edge. These two temperatures and the stress rise remarkably at a higher Mach number.

(2) If the high temperature heat pipe operates with lithium as the actuating medium, the C-103 and T-111 completely satisfy all the operative requirements with a 3 mm leading edge radius and a 0.15 m design length from Mach number 6 to 8. On the other hand the maximum von Mises stress exceeds the yield strength of Inconel 625 at a speed higher than Mach number 6, which means a material failure.

(3) Finite element method is proved to be a reliable solution as the supplement and the substitute of experiment when obtaining necessary information. However, it needs a more complex procedure before obtaining the final result and consumes more resources than the theoretical method. The fact that analytical solution compares well to the finite element method shows a feasible and reliable way of utilizing the analytical method as an initial design tool for hypersonic aircrafts. Engineers can use this theoretical method to evaluate whether they are going in the right direction and what factors should be considered in the first place.

Acknowledgements

This work is financially supported by the Foundation for Innovative Research Groups of the National Natural Science Foundation of China (No. 51121004) and the Fundamental Research Funds for the Central Universities (No. HIT.BRETIV.201315).

References

1. Rault DFG. Aerodynamic characteristics of a hypersonic viscous optimized waverider at high altitudes. *J Spacecraft Rockets* 1994;**31**(5):719–27.
2. Graves RE, Argrow BM. Aerodynamic performance of an osculating-cones waverider at high altitudes. 2001. Report No.: AIAA-2001-2960.
3. Sakurai H, Kobayasi M, Yamazaki I, Shirouzu M, Yamamoto M. Development of the hypersonic flight experimental vehicle. *Acta Astronaut* 1997;**40**(2):105–12.
4. Moses PL, Rausch VL, Nguyen LT, Hill JR. NASA hypersonic flight demonstrators-overview, status, and future plans. *Acta Astronaut* 2004;**55**(3):619–30.
5. Voland RT, Huebner LD, McClinton CR. X-43A hypersonic vehicle technology development. *Acta Astronaut* 2006;**59**(1):181–91.
6. Mallinson SG, Gai SL, Mudford NR. Leading-edge bluntness effects in high enthalpy, hypersonic compression corner flow. *AIAA J* 1996;**34**(11):2284–90.
7. Bertin JJ, Cummings RM. Fifty years of hypersonics: where we've been, where we're going. *Prog Aerosp Sci* 2003;**39**(6):511–36.
8. Santos WFN. Leading-edge bluntness effects on aerodynamic heating and drag of power law body in low-density hypersonic flow. *J Braz Soc Mech Sci* 2005;**27**(3):236–42.
9. Josyula E, Shange JS. Numerical study of hypersonic dissociated air past blunt bodies. *AIAA J* 1991;**29**(5):704–11.
10. Glass DE, Merski NR, Glass CE. Airframe research and technology for hypersonic airbreathing vehicles. 2002. Report No.: NASA/TM-2002-211752.
11. Buckley JD, Edie DD. *Carbon–carbon materials and composites*. New York: Noyes Publications; 1993. p. 267–79.
12. Ishii I, Kubota H. Two-dimensional material response of a transpiration-cooled system in a radiative/convective environment. *AIAA J* 1984;**22**(6):831. p. 831–6.
13. Rudy E. *Part V*. Compendium of phase diagram data, ternary phase equilibria in transition metal–boron–carbon–silicon systems. 1969. Report No.: AFML-TR-65-2.
14. Lu HB, Liu WQ. Investigation of thermal protection system by forward-facing cavity and opposing jet combinatorial configuration. *Chin J Aeronaut* 2013;**26**(2):287–93.
15. Libby PA, Hendricks P. Analysis of an active thermal protection system for high-altitude flight. *AIAA J* 1970;**8**(9):1671–8.
16. Niblock GA, Reeder JC, Huneidi F. Four space shuttle wing leading edge concepts. *J Spacecraft Rockets* 1974;**11**(5):314–20.
17. Colwell GT, Modlin JM. Heat pipe and surface mass transfer cooling of hypersonic vehicle structures. *J Thermophys Heat Transfer* 1992;**6**(3):492–9.
18. Glass DE, Merrigan MA, Sena JT, Reid RS. Fabrication and testing of a leading-edge-shaped heat pipe. 1998. Report No.: NASA CR-1998-208720.
19. Grover GM, Cotter TP, Erickson GF. Structure of very high thermal conductance. *J Appl Phys* 1964;**35**(6):1990–1.
20. Cotter TP. Theory of heat pipes. 1965. Report No.: LA-3246-MS.
21. Peterson GP. *An introduction to heat pipes: modeling, testing, and applications*. New York: John Wiley and Sons; 1994. p. 178–86.
22. Martin RA, Merrigan MA, Elder MG, Sena JT, Keddy ES. Analytical and experimental studies of heat pipe radiation cooling of hypersonic propulsion systems. 1992. Report No.: AIAA-1992-3809.
23. Johnson DB, Bogar TJ, Hunt JL. *Configuration development for a hydrocarbon fueled hypersonic cruise vehicle*; 2001. Report No.: AIAA-2001-1926.
24. Committee on Extension to the Standard Atmosphere (COESA). *U.S. standard atmosphere: 1976*. Washington: U.S. Government Printing Office; 1976. p. 50–73.
25. Fay JA, Riddell FR. Theory of stagnation point heat transfer in dissociated air. *J Aeronaut Sci* 1958;**25**(2):73. p. 73–85.
26. Sutton K, Graves RA. A general stagnation-point convective-heating equation for arbitrary gas mixtures. 1971. Report No.: NASA-TR-R-376.
27. Svehla RA. Estimated viscosities and thermal conductivities of gases at high temperatures. 1962. Report No.: NASA-TR-R-132.
28. Lees L. Laminar heat transfer over blunt-nosed bodies at hypersonic flight speeds. *J Jet Propul* 1956;**26**(4):259–69.
29. Tauber ME. A review of high-speed, convective, heat-transfer computation methods. 1989. Report No.: NASA-TP-2914.
30. Bertin JJ. *Hypersonic aerothermodynamics*. Washington, DC: AIAA; 1994.
31. Hoshizaki H, Wilson KH. Viscous, radiating shock layer about a blunt body. *AIAA J* 1965;**3**(9):1614–22.
32. Liu JTC, Sogame E. Radiative transfer in the low Reynolds number, blunt-body stagnation region at hypersonic speeds. *AIAA J* 1969;**7**(7):1273–9.
33. Tewfik OK, Giedt WH. Heat transfer, recovery factor, and pressure distributions around a circular cylinder normal to a supersonic rarefied-air stream. *J Aerosp Sci* 1960;**27**(10):721–9.

He Yurong is a professor and Ph.D. supervisor at School of Energy Science and Engineering, Harbin Institute of Technology, Harbin, China. She received the Ph.D. degree from the same university in 2004. Her current research interests are nanofluid, gas–solid two phase flow, fluidization and heat transfer.